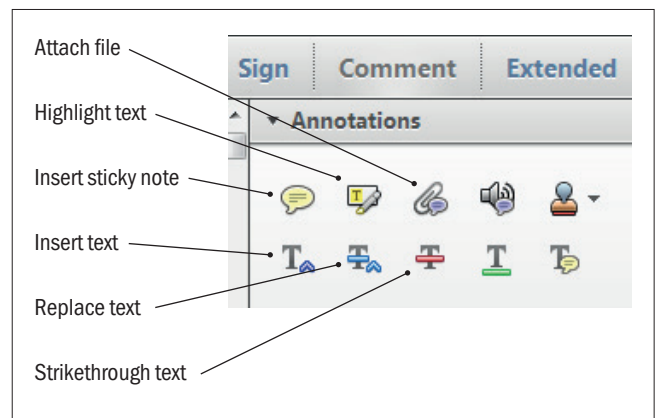


# Making corrections to your proof

Please follow these instructions to mark changes or add notes to your proof. You can use Adobe Acrobat Reader (download the most recent version from <https://get.adobe.com>) or an open source PDF annotator.

The tools you need to use are contained in **Annotations** in the **Comment** toolbar. You can also right-click on the text for several options. The most useful tools have been highlighted here. If you cannot make the desired change with the tools, please insert a sticky note describing the correction.

Please ensure all changes are visible via the 'Comments List' in the annotated PDF so that your corrections are not missed.

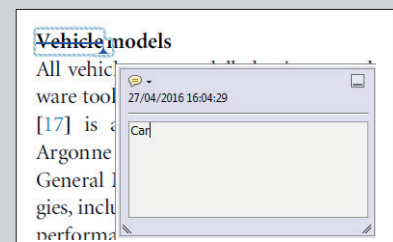


**Do not attempt to directly edit the PDF file as changes will not be visible.**



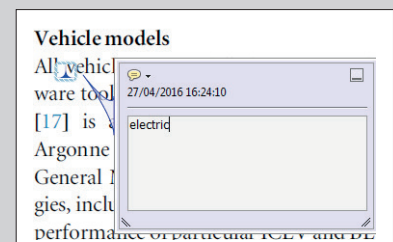
## Replacing text

To replace text, highlight what you want to change then press the replace text icon, or right-click and press 'Add Note to Replace Text', then insert your text in the pop up box. Highlight the text and right click to style in bold, italic, superscript or subscript.



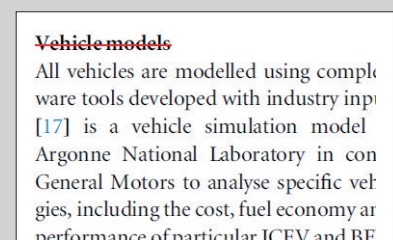
## Inserting text

Place your cursor where you want to insert text, then press the insert text icon, or right-click and press 'Insert Text at Cursor', then insert your text in the pop up box. Highlight the text and right click to style in bold, italic, superscript or subscript.



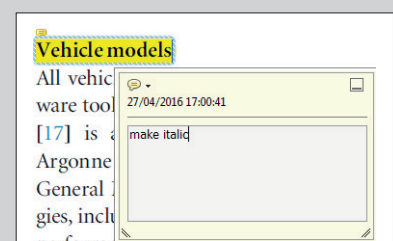
## Deleting text

To delete text, highlight what you want to remove then press the strikethrough icon, or right-click and press 'Strikethrough Text'.



## Highlighting text

To highlight text, with the cursor highlight the selected text then press the highlight text icon, or right-click and press 'Highlight text'. If you double click on this highlighted text you can add a comment.



# QUERY FORM

JOURNAL: The Astrophysical Journal

AUTHOR: Augustine et al.

TITLE: SN Ia Explosions from Hybrid Carbon–Oxygen–Neon White Dwarf Progenitors That Have Mixed During Cooling

ARTICLE ID: apjab511a

---

Your article has been processed in line with the journal style. Your changes will be reviewed by the Production Editor, and any amendments that do not comply with journal style or grammatical correctness will not be applied and will not appear in the published article.

The layout of this article has not yet been finalized. This proof may contain columns that are not fully balanced/matched or other typographical imperfections; these issues will be resolved once the final corrections have been incorporated.

Please check that the **names of all authors as displayed in the proof are correct**, and that all **authors are linked to the correct affiliations**. Please also confirm that the correct corresponding author has been indicated. **Note that this is your last opportunity to review and amend this information before your article is published.**

If you have an Acknowledgments section, please check that the information there is complete and correct and that all relevant institutions, grant numbers, programs, and collaborators are mentioned as appropriate.

---

Please check that the funding information below is correct for inclusion in the article metadata.

Department of Energy: DE-FG02-87ER40317; National Science Foundation: AST-1211563; Institute for Advanced Computational Science: N/A.

We have been provided with ORCID iDs for the authors as below. Please confirm whether the numbers are correct.

Carlyn N. Augustine 0000-0002-9741-5987

Alan C. Calder 0000-0001-5525-089X

Donald E. Willcox 0000-0003-2300-5165

Dean M. Townsley 0000-0002-9538-5948

## Page 1

Q1

Please define the acronyms [MESA & FLASH].

## Page 1

Q2

Please define the acronym [WD].

## Page 5

Q3

Please define the acronyms [EOS & CASTRO].

## Page 9

Q4

We have identified that [10.5281/zenodo.44579] is a supplementary data set, to be highlighted in the “Article data” section of the published article HTML. Is this correct? If not it will be added to the reference list. Please provide the information for the new reference citation if necessary. Please see AAS software citation policy for further questions: <https://journals.aas.org/policy-statement-on-software/>.

**Page 10**

---

Q5  
Please check the details for any journal references that do not have a link; please update with correct details and supply a CrossRef DOI or NASA ADS link if available.

**Page 10**

---

Q6  
Reference [Filippenko 1997] is repeated, so we have deleted the latter instance. Please check.

**Page 10**

---

Q7  
Please provide the publisher details in references [Harkness & Wheeler 1990, Woosley et al. 1980].

**Page 10**

---

Q8  
Please update reference [Paxton et al. 2011] if possible.

**Page 11**

---

Q9  
Please provide conference details in reference [Woosley et al. 1980]. The format for conference citations is [Publication, Conference title, editors (Publisher City, State: Publisher Name), page number].

---



# SN Ia Explosions from Hybrid Carbon–Oxygen–Neon White Dwarf Progenitors That Have Mixed During Cooling

Carlyn N. Augustine<sup>1</sup>, Donald E. Willcox<sup>2</sup>, Jared Brooks<sup>3</sup>, Dean M. Townsley<sup>1</sup>, and Alan C. Calder<sup>4,5</sup>

<sup>1</sup>Department of Physics and Astronomy, University of Alabama, Tuscaloosa, AL, 35487-0324, USA; em1

<sup>2</sup>Center for Computational Sciences and Engineering, Lawrence Berkeley National Lab, Berkeley, CA 94720, USA

<sup>3</sup>Department of Physics, University of California Santa Barbara, Santa Barbara, CA 93106, USA

<sup>4</sup>Department of Physics and Astronomy, Stony Brook University, Stony Brook, NY, 11794-3800, USA

<sup>5</sup>Institute for Advanced Computational Sciences, Stony Brook University, Stony Brook, NY, 11794-5250, USA; alan.calder@stonybrook.edu

Received 2019 August 8; revised 2019 October 25; accepted 2019 October 25; published 2019 MM DD

## Abstract

The creation of “hybrid” white dwarfs, made of a C–O core within an O–Ne shell has been proposed, and studies indicate that ignition in the C-rich central region makes these viable progenitors for thermonuclear (type Ia) supernovae. Recent work found that the C–O core is mixed with the surrounding O–Ne as the white dwarf cools prior to accretion, which results in lower central C fractions in the massive progenitor than previously assumed. To further investigate the efficacy of hybrid white dwarfs as progenitors of thermonuclear supernovae, we performed simulations of thermonuclear supernovae from a new series of hybrid progenitors that include the effects of mixing during cooling. The progenitor white dwarf model was constructed with the one-dimensional stellar evolution code MESA and represented a star evolved through the phase of unstable interior mixing followed by accretion until it reached conditions for the ignition of carbon burning. This MESA model was then mapped to a two-dimensional initial condition for explosions simulated with FLASH. For comparison, similar simulations were performed for a traditional C–O progenitor white dwarf. By comparing the yields of the explosions, we find that, as with earlier studies, the lower C abundance in the hybrid progenitor compared to the traditional C–O progenitor leads to a lower average yield of  $^{56}\text{Ni}$ . Although the unmixed hybrid WD showed a similar decrement also in total iron-group yield, the mixed case does not and produces a smaller fraction of iron-group elements in the form of  $^{56}\text{Ni}$ . We attribute this to the higher central density required for ignition and the location, center or off-center, of deflagration ignition.

*Unified Astronomy Thesaurus concepts:* Explosive nucleosynthesis (503); Type Ia supernovae (1728); Hydrodynamical simulations (767); White dwarf stars (1799);

## 1. Introduction

Thermonuclear (Type Ia) supernovae (SNe Ia) are bright stellar explosions thought to occur when approximately  $1.0 M_{\odot}$  of material composed principally of C and O burns under degenerate conditions. This class of supernovae is known to synthesize much of the Fe-group elements found in the galaxy, and the light curves of these events have a special property that allows standardization as distance indicators for cosmological studies (Phillips 1993). This use resulted in the discovery of the acceleration of the expansion of the universe and thus the inference of dark energy (Riess et al. 1998; Perlmutter et al. 1999; Leibundgut 2001), and these events remain critical distance indicators for cosmological studies (Weinberg et al. 2013). The special property of the light curve is thought to follow from the fact that the source of luminosity, the radioactive decay of  $^{56}\text{Ni}$  synthesized by the thermonuclear burning, is also the principal source of opacity (Pinto & Eastman 2001), giving the Phillips relation between the brightness of an event and the rate of decline of the B-band magnitude from maximum (Phillips 1993).

Supernovae are classified observationally by their light curves and spectra (Minkowski 1941; Bertola 1964; Porter & Filippenko 1987; Harkness & Wheeler 1990; Filippenko 1997), with the type Ia designation following from the absence of H in the spectrum and the presence of a specific Si line (Filippenko 1997; Hillebrandt & Niemeyer 2000). These events have been associated with C burning under degenerate conditions for some time (Hoyle & Fowler 1960; Arnett et al. 1971), but

discerning the setting(s) of these events is proving difficult and remains the subject of active research. At present there are three widely accepted scenarios: the single degenerate scenario, the double detonation or sub-Chandrasekhar scenario, and the white dwarf merger scenario. We briefly describe these in the subsection that follows. Also see Hillebrandt & Niemeyer (2000), Howell (2011), Hillebrandt et al. (2013), Calder et al. (2013), Seitenzahl & Townsley (2017), and Röpke & Sim (2018) for additional discussion. We note that hybrid white dwarfs are particularly interesting to the single degenerate picture because the greater mass of a hybrid WD might resolve a concern.

### 1.1. Proposed Progenitor Settings

The single degenerate picture posits a white dwarf gaining mass from a companion, and the process relies on a long period of accretion combined with either steady burning or a series of nova explosions for a traditional C–O WD to gain the  $\sim 0.4 M_{\odot}$  needed for it to approach the limiting Chandrasekhar mass (Starrfield et al. 2012). As the WD approaches the Chandrasekhar limit, conditions in the compressed core are right to ignite the thermonuclear burning that will incinerate the star. Within this progenitor setting, models that best reproduce observations are those in which the burning begins as a subsonic deflagration during which the star expands that is then followed by supersonic detonation (Khokhlov 1991; Höflich & Khokhlov 1996; Gamezo et al. 2005; Calder et al. 2013; Hillebrandt et al. 2013). We simulate thermonuclear explosion

properties assuming this scenario and describe our methodology in detail below.

The double detonation picture also has a white dwarf gaining mass from a companion. The supernova begins with a detonation occurring in an accreted layer of He, and that subsequently triggers another detonation in the underlying white dwarf (Nomoto 1980, 1982; Taam 1980a, 1980b; Woosley et al. 1980). Early studies indicated that this scenario could work for a wide range of white dwarf masses, not just the near-Chandrasekhar case (Livne 1990), hence the moniker “sub-Chandrasekhar” also applied to this scenario (Woosley & Weaver 1994). The mass of accreted He is a concern because heavier elements synthesized in the He detonation will appear in the outer ejecta, which does not match observations (Höflich et al. 1996; Höflich & Khokhlov 1996; Fink et al. 2007; Sim et al. 2010). Bildsten et al. (2007), however, found that fairly thin He layers could flash on sub-Chandrasekhar mass white dwarfs, encouraging further research (Sim et al. 2012; Brooks et al. 2015; Glasner et al. 2018; Shen et al. 2018; Townsley et al. 2019).

The white dwarf merger progenitor picture has two white dwarfs coming together and subsequently exploding (Tutukov & Iungelson 1976; Tutukov & Yungelson 1979; Iben & Tutukov 1984; Webbink 1984). This scenario provides an abundance of degenerate fuel, which may explain some bright events (Scalzo et al. 2010; Yuan et al. 2010). Early modeling efforts found that as the stars merge, the more massive white dwarf can ignite near its edge and fail to produce a supernova (Saio & Nomoto 1985, 2004; Shen et al. 2012). Subsequent work allayed this concern by demonstrating that a low accretion rate from the disrupted secondary,  $< 3 \times 10^{-6} M_{\odot}$  per year, did not heat the primary enough for ignition (Kawai et al. 1987; Saio & Nomoto 2004; Yoon et al. 2007; Lorén-Aguilar et al. 2009; Pakmor et al. 2012a). Contemporary research focuses on variations on the merger idea, including inspiraling pairs, collisions, violent mergers, and the “core-degenerate” model in which the merger takes place in a common envelope (Raskin et al. 2009; Kashi & Soker 2011; Pakmor et al. 2011, 2012b; Shen et al. 2012; Katz et al. 2016; Brooks et al. 2017b).

### 1.2. The Deflagration to Detonation Transition Mechanism Within the Single Degenerate Scenario

The approach we employ for this study is a variation of the delayed detonation described above, the deflagration-to-detonation transition (DDT) explosion paradigm (Blinnikov & Khokhlov 1986; Khokhlov 1991; Niemeyer & Woosley 1997; Niemeyer 1999; Bell et al. 2004; Fisher & Jumper 2015). In this case, the accretion of mass on the white dwarf compresses and heats the core, igniting carbon fusion and driving a period of convection (Woosley et al. 2004; Wunsch & Woosley 2004; Kuhlen et al. 2006; Nonaka et al. 2012). At some point, the fusion rate becomes fast enough due to the rising temperature that energy production exceeds convective cooling and the deflagration phase begins in the core (Nomoto et al. 1984; Woosley et al. 2004).

This flame is unstable, and as the deflagration propagates toward the surface of the WD, it is subject to the Rayleigh–Taylor instability that generates turbulence and boosts burning (Taylor 1950; Chandrasekhar 1981). Burning proceeds as a deflagration for about one second, and then the flame transitions to a detonation (Höflich et al. 1995). Our

simulations assume that the transition occurs when the top of a rising Rayleigh–Taylor unstable plume reaches a characteristic low density (Townsley et al. 2007).

In the DDT paradigm, the duration of the deflagration phase sets the amount of expansion of the star prior to the bulk of burning, which is critical to the composition of material synthesized in the explosion. Also, early burning during the deflagration phase is at high enough densities that the effects of electron capture are significant and similarly influence the composition of the material synthesized in the explosion (Höflich et al. 2004; Höflich 2006; Fesen et al. 2007; Diamond et al. 2018).

### 1.3. A Recent Advance in Stellar Evolution: Hybrid White Dwarfs

Modern computing resources now enable simulations with unprecedented realism, allowing both one-dimensional simulations with a vast amount of included physics and full three-dimensional simulations albeit with less included physics (Calder & Townsley 2019, and references therein). In the area of stellar evolution, recent investigations revisiting late-time evolution of roughly  $8 M_{\odot}$  stars indicate that under the right circumstances, “hybrid” white dwarfs having a C–O core surrounded by O–Ne mantle may form (Siess 2009; Denissenkov et al. 2013). These hybrid white dwarfs are thought to form when mixing at the lower convective boundary quenches C burning in an asymptotic giant branch star, leaving unburned C in the core. The situation is at best uncertain, however, and the results depend on assumptions about convective overshoot that have been questioned (Chen et al. 2014; Lecoanet et al. 2016; Lattanzio et al. 2017).

These hybrid WDs are relevant to the supernova problem because they can become the progenitors of thermonuclear supernovae if they are part of a binary system. If the companion star becomes another WD, the two can merge and produce an explosion. If, on the other hand, the hybrid WD has a main sequence or giant companion, it can gain mass and approach the Chandrasekhar mass, i.e., the single degenerate picture (Willcox et al. 2016).

In any case, the hybrid WD will experience a period of cooling, which will reduce the stabilizing temperature gradient (the O–Ne layer is initially hotter than the C–O core) and allow the unstable composition gradient to drive thermo-compositional convection (Brooks et al. 2017a; Schwab & Garaud 2019). In the case of the hybrid WD accreting and approaching the Chandrasekhar mass, accretion will heat the core and start C fusion, leading to a period of “simmering” prior to the explosion, also mixing the interior (Piro & Bildsten 2008). The upshot is that there is likely to be considerable mixing after the hybrid forms that will homogenize the composition (Denissenkov et al. 2015; Brooks et al. 2017a; Schwab & Garaud 2019).

Hybrid WDs have more mass than traditional C–O WDs, with some studies indicating the mass can approach  $1.3 M_{\odot}$  (Chen et al. 2014). This increased mass minimizes one of the problems associated with the single degenerate picture, the need to accrete enough mass for the WD to approach the Chandrasekhar mass (Chen et al. 2014; Denissenkov et al. 2015; Kromer et al. 2015). Accordingly, there has been considerable interest in viability of explosions from these progenitors.



From population synthesis, Meng & Podsiadlowski (2014) found that these progenitors may substantially contribute to the population of SNe Ia (1%–8%) and have relatively short delay times. They also suggested that these may produce part of the Iax class of events. Wang et al. (2014), also with population synthesis, studied the case of a hybrid progenitor accreting from a non-degenerate He star and found birth rates indicating that up to 18% of SNe Ia may follow from this channel and very short delay times. Wang et al. (2014) also suggested that explosions from hybrid progenitors may provide an explanation for type Iax events. Meng & Podsiadlowski (2018), from the common-envelope-wind model developed in Meng & Podsiadlowski (2014), propose that both Ia-CSM and Iax events are caused by the explosion of hybrid progenitors, with Ia-CSM occurring in systems with a massive common envelope and Iax events occurring in systems where most of the common envelope has been lost.

Other groups have simulated explosions from hybrid progenitors. Kromer et al. (2015) performed pure deflagration simulations from models with a C core. They found that their models may explain some faint events such as SN 2008ha (Foley et al. 2009). Interpretation of these results are made challenging by their use of a progenitor in which no mixing has occurred, not even that expected due to simmering. Bravo et al. (2016) performed one-dimensional simulations of explosions from a variety of progenitor models assuming both pure deflagration and the DDT explosion mechanism. Some of their models are similar to those of Denissenkov et al. (2015) and they report that many models produce less synthesized  $^{56}\text{Ni}$ , indicating dimmer events. They also note that some of their models may explain Iax events. Willcox et al. (2016) simulated explosions from the progenitors of Denissenkov et al. (2015) and found lower  $^{56}\text{Ni}$  yields on average and a trend of lower ejecta kinetic energy when compared to explosions from traditional C–O progenitors. We will compare to the work of Willcox et al. (2016) extensively below. They did not allow for the mixing of the WD during cooling, before ignition of carbon burning. Here we utilize progenitors in which mixing during cooling has been modeled appropriately (Brooks et al. 2017a).

Discerning the role played by hybrid progenitors in the global gamut of thermonuclear supernovae is the goal of the study we present in this paper. Our simulations provide the yields of  $^{56}\text{Ni}$  in the supernova explosions. Because the radioactive decay of  $^{56}\text{Ni}$  powers the light curve of an event, the yield of  $^{56}\text{Ni}$  serves as a proxy for brightness of the event so our estimates allow us to discern trends in brightness. Our study thus can offer insight into the relative brightness of explosions from these progenitors as well as the overall scatter in the brightness of observed events.

Our simulation methodology is described in the next section and our results include a comparison of nucleosynthetic explosion yields between these new mixed hybrid C–O–Ne progenitors and traditional C–O progenitors in the section following the methodology. Our results show systematic differences in the yield of  $^{56}\text{Ni}$  between explosions from the two types of progenitors, which we quantify and discuss.

## 2. Methodology

The methodology of our study follows the approach of Willcox et al. (2016). We performed a suite of two-dimensional simulations of supernova explosions from hybrid progenitors and compared the results to a suite of simulations of explosions

from traditional C–O progenitor models performed with the same simulation code and from similar initial conditions. The simulations assumed the DDT explosion paradigm, and the transition densities were the same in both suites. We briefly review our methodology here, and refer the reader to previous work for additional details. In particular, we use the same simulation instrument, a modified version of the FLASH code, as Willcox et al. (2016) and we refer the reader there for a description of the process and treatment of burning of C–O–Ne fuel and how it differs from C–O fuel.

### 2.1. Simulation Instrument

The simulations of supernova explosions presented here were performed with a customized version of the FLASH code, originally developed at the University of Chicago. FLASH is a parallel, adaptive mesh, multi-physics simulation code developed first for nuclear astrophysics applications and subsequently for high-energy-density applications (Calder et al. 2000, 2002; Fryxell et al. 2000; Dubey et al. 2013, 2014). FLASH has been applied to a variety of astrophysical problems by a host of researchers, and the version we apply differs from other versions principally in the modules describing thermonuclear burning via a flame capturing model.

The need for a model flame in simulating thermonuclear supernovae follows from the scales of the problem. At high densities, the width of a laminar nuclear flame is  $<1$  cm while the radius of the white dwarf is  $\sim 10^9$  cm. Even with adaptive mesh refinement, whole-star simulations cannot simultaneously resolve the nuclear flame, so simulations require a model to describe the burning on unresolved scales. The model we apply is a flame capturing scheme and thermally activated burning module to describe thermonuclear burning during both the deflagration and detonation phases, as well as routines to describe the evolution of the dynamic ash. This description of the burning was developed during the course of research in thermonuclear supernovae and has been presented in a series of papers (See Townsley et al. 2016; Calder et al. 2017, and references therein). For completeness, we briefly review the flame capturing scheme here.

For the deflagration phase, the flame capturing scheme propagates an artificially broadened flame with an advection-diffusion-reaction (ADR) scheme (Khokhlov 1995; Vladimirova et al. 2006) via evolution of a reaction progress variable to describe the consumption of C and additional variables to describe the evolution of intermediate-mass elements into the statistical quasi-equilibrium of the Si-group (Imshennik et al. 1981; Khokhlov 1981, 1983) and then into iron-group elements (IGEs) in full nuclear statistical equilibrium (NSE).

The reaction progress variable is  $\phi$  and it varies from  $\phi = 0$  for unburned fuel to  $\phi = 1$  for burned ash.  $\phi$  is evolved via an ADR equation,

$$\partial_t \phi + \mathbf{u} \cdot \nabla \phi = \kappa \nabla^2 \phi + \frac{1}{\tau} R(\phi), \quad (1)$$

where  $\mathbf{u}$  is the velocity of the fluid,  $\kappa$  is the diffusion coefficient,  $\tau$  is the reaction timescale, and  $R(\phi)$  is a non-dimensional function describing the reaction. The parameters  $\kappa$ ,  $\tau$ , and  $R(\phi)$  are tuned to propagate the reaction front at a prescribed speed. Our model uses the “sharpened KPP” described by Vladimirova et al. (2006), with  $R \propto (\phi - \epsilon)(1 - \phi + \epsilon)$ , where  $\epsilon \simeq 10^{-3}$ . This scheme has been shown to be



acoustically quiet, stable, and to give a unique flame speed (Townsend et al. 2007). The input flame speeds come from tabulated results obtained by direct numerical simulations of thermonuclear burning. The flame speeds are obtained via linear interpolation within a three-dimensional table that combines the results of Timmes & Woosley (1992) and Chamulak et al. (2008), and the dimensions of the table are  $^{12}\text{C}$  mass fraction,  $^{22}\text{Ne}$  mass fraction and log of density. While the WD contains additional species, we have shown that treating the abundance of  $^{22}\text{Ne}$  as a proxy for neutron-rich elements captures the speed-up of laminar flames due to neutronization and thus reasonably produces variations in flame speed due to composition (Jackson et al. 2010). Using these tables, which were made for mixtures without  $^{20}\text{Ne}$ , effectively assumes that the substitution of  $^{20}\text{Ne}$  for  $^{16}\text{O}$  will not change the flame speeds significantly. We consider this a reasonable approximation given that, in the interior of our star,  $^{16}\text{O}$  is still much more abundant than  $^{20}\text{Ne}$ , and that the flame propagation is largely dominated by turbulent effects. These laminar flame speeds are boosted to account for the speed-up of burning due to unresolved buoyancy and background turbulence (Khokhlov 1995; Gamezo et al. 2003; Townsend et al. 2007; Jackson et al. 2014).

The two-dimensional models in this study do not utilize a sub-grid-scale model for the turbulence-flame interaction (See Schmidt et al. 2006a, 2006b; Jackson et al. 2014, for examples). Those sub-grid-scale models only apply in three-dimensional simulations because two-dimensional hydrodynamics cannot correctly describe turbulence. The simulations we present use the minimal enhancement based on the Rayleigh–Taylor strength introduced by Townsend et al. (2007). The assumption here is that the burning self-regulates on resolved scales so that results are insensitive to the detailed treatment of the interaction with turbulence, and previous experience indicates this assumption is reasonable for comparisons like the one presented in this work (Townsend et al. 2007; Willcox et al. 2016).

The ADR scheme describes the consumption of C and the subsequent stages are described by separate progress variables and separate relaxation times derived from full nuclear network calculations (Calder et al. 2007; Townsend et al. 2016). In both the quasi-equilibrium and full equilibrium, the creation of light elements by photodisintegration balances the creation of heavy elements by fusion, maintaining the equilibrium. The relative balance depends on thermodynamic conditions, e.g., density and temperature, and hydrodynamic motion during the explosion changes the thermodynamic conditions, and thus the balance. Electron capture also influences the evolution in several ways by neutronizing the material, which produces more neutron-rich iron-group material at the expense of  $^{56}\text{Ni}$ . Neutronization also shifts the binding energy of the material and the Fermi energy of electrons, respectively changing the temperature (due to released energy) and the pressure. Finally, individual electron capture reactions emit neutrinos that escape and remove energy from the system. Like the input flame speed, the burning model includes tabulated rates for these effects from detailed NSE calculations (Seitenzahl et al. 2009). Accordingly, the burning model is able to describe dynamic evolution of the ash in addition to the stages of C–O–Ne burning.

The burning model also describes the detonation phase with progress variables. In this case, the model evolves thermally activated burning with the actual temperature-dependent rate for C consumption, which allows a propagating shock to trigger burning, i.e., to propagate a detonation front. The propagating detonation is able to describe the same stages of C burning as the deflagration case, including the relaxation into NSE (Townsend et al. 2016, and references therein). Finally, we again note that the burning model was adapted for the case of burning in hybrid white dwarfs. Parameter studies of detonations in C–O–Ne material and details of how the burning model is used to capture C–O–Ne burning may be found in Willcox et al. (2016).

## 2.2. One-dimensional Hybrid Model

The hybrid white dwarf model that served as the initial condition for the simulations of supernova explosions presented in this work was constructed with the one-dimensional stellar evolution code MESA (Paxton et al. 2011, 2013, 2015, 2016). The evolution of the model included larger nuclear reaction networks than previous studies and thus resulted in an electron-to-baryon gradient that became unstable to mixing as the interior cooled, leading to a lower central C fraction than previous hybrid models (Brooks et al. 2017a). We selected the  $1.09 M_{\odot}$  WD model with the  $0.4 M_{\odot}$  C/O core from Brooks et al. (2017a). In order to grow this WD towards the Chandrasekhar mass, it was inserted into a binary with a  $1.4 M_{\odot}$  He star donor having a 3 hr orbital period, similar to the simulations in Brooks et al. (2016), and the system was allowed to evolve. The WD grows, experiences central carbon ignition and simmering, and then is stopped when its central temperature reaches  $\log T_c(\text{K}) = 8.9$ , at which point the temperature is just about high enough to ignite the deflagration that is the first stage of the explosion. The central  $^{12}\text{C}$  mass fraction of the model is 0.1419.

Following the approach of Willcox et al. (2016), we constructed a corresponding “classic” C–O model to allow comparison of explosion results between these hybrid models and those of previous studies (Krueger et al. 2010, 2012). The C–O model was constructed to have conditions as similar as possible to the hybrid model (e.g., the two shared the same central temperature and density). The central  $^{12}\text{C}$  mass fraction of this model is 0.4. Figure 1 shows the density and temperature profiles of the two initial one-dimensional models. While the C–O–Ne progenitor is the result of an evolutionary calculation, the C–O progenitor is constructed by integrating the equation of hydrostatic equilibrium using the Helmholtz stellar equation of state of Timmes & Swesty (2000) starting from the central density and temperature of the C–O–Ne WD model. This parameterized construction is reflected in the simplified outer thermal structure for the C–O WD model appearing in Figure 1. We centrally ignite our explosion simulations for both C–O and hybrid models to coincide with the peak temperature at the center of the WDs, unlike the hybrid models of Willcox et al. (2016).

## 2.3. Two-dimensional Initial Conditions From One-dimensional Models

The initial progenitor models for the two-dimensional simulations were created from the one-dimensional MESA models by mapping the one-dimensional models onto the

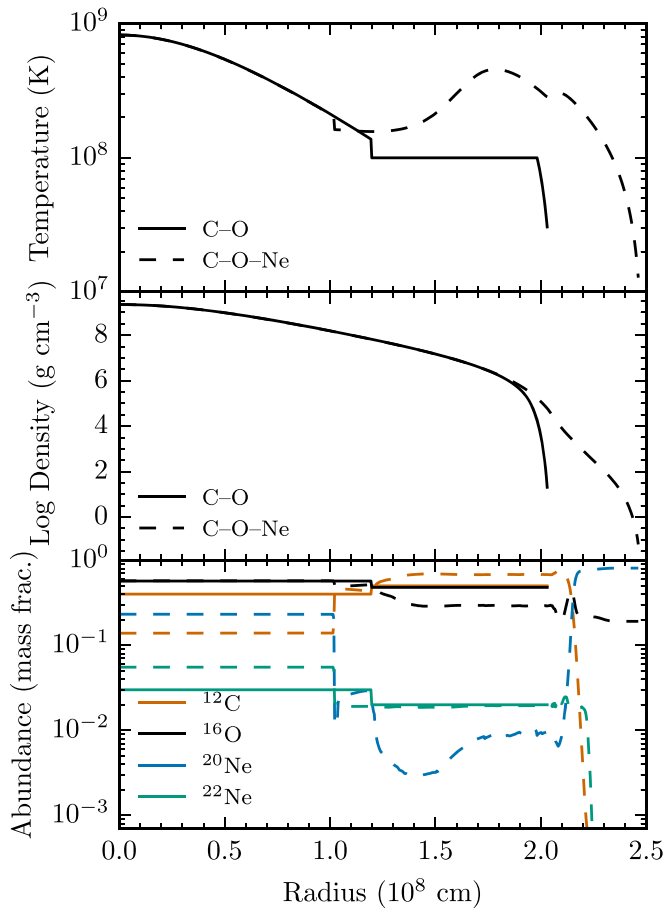


**Figure 1.** Radial temperature, density, and composition profiles of the one-dimensional hybrid progenitor WD. The central temperature and density were the same as the traditional C-O progenitor model. The peak temperature of the hybrid model is at the center of the star, so both the hybrid and C-O models could share the same central ignition initial conditions in our simulations.

two-dimensional domain while preserving hydrostatic equilibrium. As described above, the flame capturing scheme with progress variables describes the evolution as the material burns. The MESA models, however, relied on a detailed reaction network that included many species. Accordingly, the process of creating the two-dimensional models for FLASH required aggregating some of the species abundances. As with much of this study, we applied the techniques of Willcox et al. (2016).

The process of mapping the MESA models began by converting the MESA model to a uniform grid of 4 km resolution. To do this, MESA quantities were mass-weighted and averaged in zones with spacing less than 4 km and interpolated in zones with spacing greater than 4 km. At this point, abundances of nuclides from the MESA models were aggregated into the abundances tracked by the flame capturing scheme in FLASH. The most abundant isotopes in the model were  $^{12}\text{C}$ ,  $^{16}\text{O}$ , and  $^{20}\text{Ne}$ , which are symmetric (the number of neutrons equals the number of protons). Similarly to Willcox et al. (2016), other neutron-rich isotopes in the initial model were combined into  $^{22}\text{Ne}$ , which serves as a proxy for metallicity. The aggregation accounts for the  $Y_e$  of the full set of nuclides, and  $^{20}\text{Ne}$  and  $^{16}\text{O}$  were constrained to be in the same ratio in both sets of abundances. Figure 1 shows the initial profile of the one-dimensional models.

The original MESA model was in equilibrium, but to ensure the uniformly gridded model was in hydrostatic equilibrium we

constructed the appropriate pressure profile. This was done by integrating for the pressure in each zone from the central point up, accounting for the local acceleration of gravity, temperature, composition, and the mass below and enclosed by the zone. As with Willcox et al. (2016), we used the EOS routine from CASTRO (Timmes & Swesty 2000; Almgren et al. 2010). This procedure produced a structure that was stable in FLASH, with fluctuations in central density less than 3%, for at least 5 s with no energy deposition.

#### 2.4. DDT Process and Suites of Explosions

The simulations performed for this study consisted of a suite of 30 two-dimensional simulations of thermonuclear supernova explosions from hybrid C-O-Ne progenitors in the DDT explosion paradigm. These were compared to a suite of supernova simulations from traditional C-O progenitors. The C-O progenitors are parameterized and include the effects of convective “simmering” in the core as the WD approaches the Chandrasekhar mass (Chamulak et al. 2008; Piro & Bildsten 2008; Jackson et al. 2010). Using parameterized C-O models allowed us to choose conditions, e.g., central density, to control differences between the hybrid and traditional models and thus assess the effect of the hybrid structure. The central density at ignition depends on both the carbon abundance and the binary history, mainly cooling time before accretion (Krueger et al. 2012), and so this comparison does not correspond to a comparable binary scenario, but is intended as a more straightforward comparison.

The C-O and C-O-Ne models have the same central temperature and density,  $8.2 \times 10^8$  K and  $2.2 \times 10^9$  g cm $^{-3}$ , respectively. The C-O model’s composition consisted of  $^{12}\text{C}$ ,  $^{16}\text{O}$ , and  $^{22}\text{Ne}$  in mass fractions 0.4, 0.57, and 0.02 respectively in the convective core, and 0.5, 0.48, and 0.02 outside the convective core. The C-O-Ne model used in FLASH had composition consisting of  $^{12}\text{C}$ ,  $^{16}\text{O}$ ,  $^{20}\text{Ne}$ , and  $^{22}\text{Ne}$ . The mass fractions in the central convection zone were 0.14, 0.68, 0.23, and 0.05 respectively, and vary smoothly outside the convection zone as shown in Figure 1.

In both suites, the simulation begins with a progenitor model mapped to the two-dimensional FLASH grid. The burning is initiated with a “match head,” a region in the white dwarf’s center that is fully burned to NSE. This initially burned region ignites a deflagration, a subsonic flame, and because the match head was perturbed it is unstable to the Rayleigh–Taylor instability with the result that buoyant plumes rise. The star is partially consumed during this deflagration phase, and the star responds by expanding. When a plume reaches a specified density, a detonation is initiated, and the simulation continues until the expanding star reaches low densities, at which point burning effectively ends. This section provides details of the implementation of this method.

The simulations were performed in two-dimensional  $r$ - $z$  cylindrical coordinates, extending radially from 0 to 65,536 km and along the axis of symmetry from  $-65,536$  km to 65,536 km. The maximum refinement level of the adaptive mesh corresponded to 4 km resolution, which previous studies have shown is a good balance between efficiency and accuracy (Townsend et al. 2007, 2009). This resolution and geometry was used in previous studies allowing direct comparison to previous results (Krueger et al. 2012).

The ignition of the deflagration via a match head followed the initialization described in Krueger et al. (2012), which

Q3



followed the method of Townsley et al. (2009). In both the hybrid and traditional cases, the match head had a nominal radius of 150 km before a different **randomly seeded** perturbation was applied to the match head for each of the 30 simulations in both **suites**. The perturbation to the sphere’s surface is a set of spherical harmonic functions with randomly chosen amplitudes, and each set of perturbations is referred to as a “realization.” Both suites use the same 30 realizations of the ignition geometry. These perturbations have been shown to reproduce the scatter in  $^{56}\text{Ni}$  yield from **SNe Ia** (Townsley et al. 2009). We note that the ignition points of the hybrid models of Willcox et al. (2016) substantially differed from both the (mixed) hybrid models presented here and traditional models. Those progenitors had the highest temperatures and hence were ignited at a radius of about 300 km.

The **DDT** again follows the previous studies, which assumed the transition location is parameterized by the fuel density  $\rho_{\text{DDT}}$ . When a rising plume reaches the threshold density, in this case  $\rho_{\text{DDT}} = 10^{7.2} \text{ g cm}^{-3}$ , a 12 km radius region of **fuel** is fully burned 32 km radially outwards from the flame. This instantaneous burning in the region of this size provides conditions to generate the shock and support the detonation at the chosen threshold density. Multiple DDT points may arise, but they are constrained to be at least 200 km apart. The choice of DDT in the suite has been shown to be high enough to ensure the robust ignition of a detonation shock.

Once the detonation starts, the remaining fuel at densities high enough for the detonation to propagate is quickly consumed. The simulations were run to 4.0 s, by which time burning has effectively ceased.

### 3. Results

We frame the presentation of the results of the suites of simulations principally in terms of the yield of  $^{56}\text{Ni}$ , the energy source of the light curve of an event.  $^{56}\text{Ni}$  thus serves as a proxy for the brightness of an explosion and comparison of the yields is equivalent to comparing the brightness of events. The yields were estimated from  $Y_e$  and the NSE progress variable, by assuming the composition upon NSE freeze-out is  $^{56}\text{Ni}$  plus equal parts  $^{54}\text{Fe}$  and  $^{58}\text{Ni}$  (Townsley et al. 2009; Meakin et al. 2009). This assumption allows the fraction of IGEs in the form of  $^{56}\text{Ni}$  to be estimated from the  $Y_e$  tracked by the burning model. This process has been shown to provide estimated  $^{56}\text{Ni}$  yields consistent with the results of detailed network and NSE calculations (Townsley et al. 2016; Calder & Townsley 2019).

The cumulative distribution of the  $^{56}\text{Ni}$  yield for explosions from **C–O** and hybrid **C–O–Ne** models is presented in Figure 2. Average and standard deviations of the sample of yields and kinetic energies are given in Table 1. The figure shows that the hybrid models consistently have a higher cumulative fraction at a given mass of  $^{56}\text{Ni}$ , which indicates that the yields of  $^{56}\text{Ni}$  are consistently lower in explosions from hybrid progenitors of the same central density. This contrast is in a similar direction but not as large as the difference between **C–O** and **C–O–Ne** progenitors seen in Willcox et al. (2016).

The production of  $^{56}\text{Ni}$ , after NSE freeze-out, as a function of simulation time for 10 simulations of explosions from each progenitor is shown in Figure 3. The sharp increase in the yield occurring after approximately 1.0 s indicates the transition to the detonation phase with its significantly faster burning. The curves indicate that on average, the **C–O–Ne** models reach the

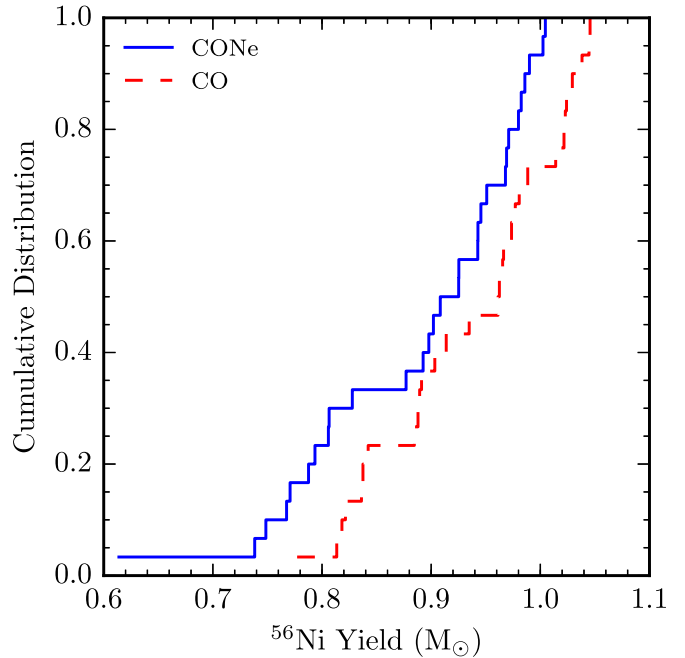


**Figure 2.** Cumulative distribution of the final  $^{56}\text{Ni}$  yield for explosions from **C–O** (red) and hybrid **C–O–Ne** (blue) models. The curve for the hybrid models is shifted to the left, indicating that explosions from hybrid progenitors produce less  $^{56}\text{Ni}$  than explosions from traditional **C–O** models with the same central density.

**Table 1**  
Average Yields and Kinetic Energies

Progenitor	$^{56}\text{Ni}$ ( $M_{\odot}$ )	IGE ( $M_{\odot}$ )	Kinetic Energy ( $10^{51}$ erg)
C–O	$0.94 \pm 0.08$	$1.14 \pm 0.08$	$1.35 \pm 0.06$
C–O–Ne	$0.89 \pm 0.10$	$1.15 \pm 0.11$	$1.21 \pm 0.07$

DDT later than the hybrid model, implying more expansion of the WD and lower density burning in the detonation phase.

Figure 4 compares the final yield of IGEs for the **C–O** and **C–O–Ne** simulation suites with the amount of expansion of the WD during the deflagration phase. The amount of expansion is characterized by the mass above  $2 \times 10^7 \text{ g cm}^{-3}$  at the time of the first DDT occurrence, with more high-density mass indicating less expansion during deflagration (Townsley et al. 2009). The averages and standard deviations,  $\sigma$ , of both the **C–O** and **C–O–Ne** suites along both axes are indicated by the shaded regions with  $\pm 1\sigma$  widths. Lighter shaded regions indicate the averages and standard deviations found by Willcox et al. (2016) for hybrid **C–O–Ne** progenitors that do not mix during cooling and for **C–O** progenitors with the same central density as them.

As expected from previous studies (e.g., Townsley et al. 2009), the trend for both **C–O** and **C–O–Ne** models is that less expansion during the deflagration phase results in greater IGE yields. This is because less expansion allows the detonation to consume more **high-density** fuel, which is burned more completely (see discussion in Seitenzahl & Townsley 2017, and references therein). At moderate expansion, where the mass at high density is between around  $1.0\text{--}1.1 M_{\odot}$ , our **C–O** models tend to yield greater IGE mass. Following Willcox et al. (2016), we interpret the lower IGE yield in **C–O–Ne** models in this range as resulting from the lower  $^{12}\text{C}$  abundance and the

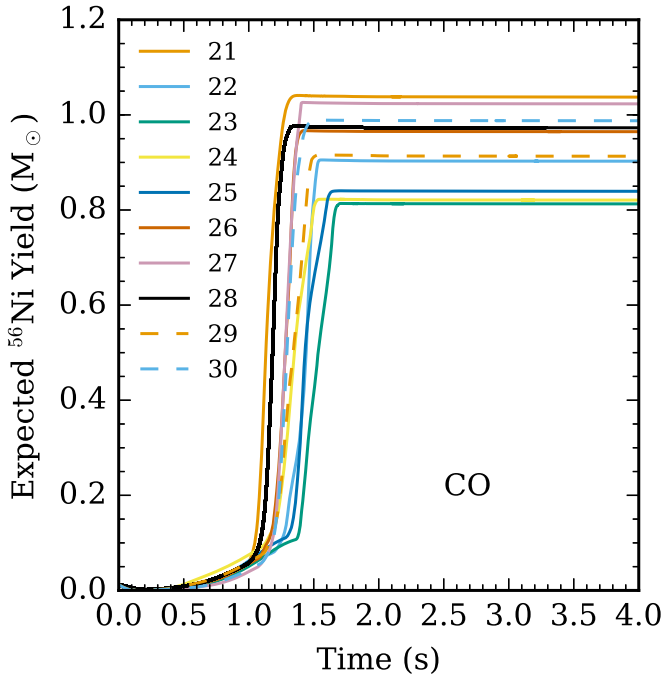
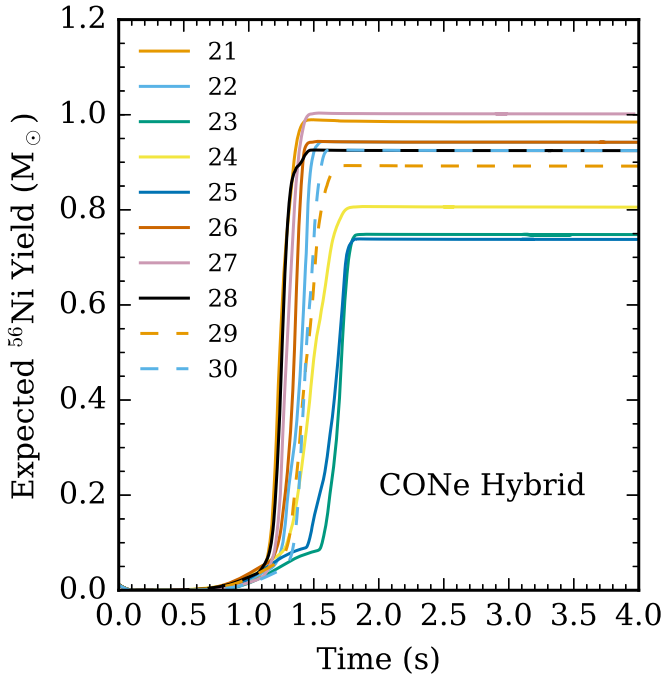


**Figure 3.** Evolution of expected  $^{56}\text{Ni}$  yield in time for 10 hybrid  $\text{C-O-Ne}$  WD (top panel) and 10  $\text{C-O}$  WD (bottom panel) explosion simulations. Shown are realizations 21–30.

fact that, given similar fuel density, the  $^{20}\text{Ne}$ -rich fuel will burn to cooler temperatures than fuel in the  $\text{C-O}$  models. The result is slower burning to IGE and thus a lower IGE yield. At lower degrees of expansion, where there is around  $1.2 M_{\odot}$  of material at high densities, there appears to be little difference between the IGE yields of  $\text{C-O}$  and  $\text{C-O-Ne}$  progenitors. This convergence for dense, weakly expanded, cases was not noted in Willcox et al. (2016) because they had very few cases with more than  $1.1 M_{\odot}$ . It does appear consistent with an

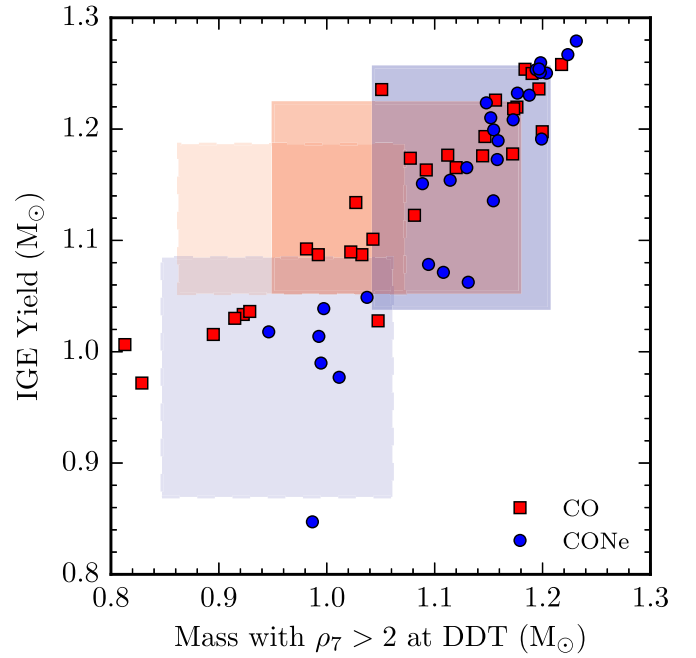


**Figure 4.** Final IGE yield vs. mass above  $2 \times 10^7 \text{ g cm}^{-3}$  at the time of the first DDT in a simulation. Individual realizations are shown ( $\text{C-O-Ne}$  progenitors in blue,  $\text{C-O}$  in red) along with rectangles of length  $\pm 1\sigma$  along each axis and centered at their average values for  $\text{C-O}$  and  $\text{C-O-Ne}$ . Similar rectangles found in Willcox et al. (2016) for a progenitor without mixing during cooling are shown in a lighter shade with dashed borders.

extrapolation of their data and their two cases that did yield these higher masses at high density.

This convergence of IGE yield also appears strongly in comparing the averages over the whole set found in this study and that of Willcox et al. (2016). As seen from the shaded regions in Figure 4 (lighter shade is unmixed), the degree of expansion seen for the our mixed progenitors is significantly less than for the unmixed cases. This results in more mass at high density in the mixed cases, leading the  $\text{C-O-Ne}$  case to produce a similar amount of IGE, on average, to the  $\text{C-O}$  case.

There are two major differences between the explosions computed in Willcox et al. (2016) and here. First, the central density of the progenitor that mixed during cooling is about 60% higher than that of the unmixed one,  $2.2 \times 10^9 \text{ g cm}^{-3}$  compared to  $1.4 \times 10^9 \text{ g cm}^{-3}$ . This is due to the higher central density necessary to ignite carbon burning with the lower central carbon fraction resulting from mixing during cooling (Brooks et al. 2017a; Section 2 above). Second, while the case without mixing during cooling led to an off-center ignition of the deflagration, here the mixed case ignited at the center. We conclude that each of these contribute in specific ways to the differences between the results of mixed and unmixed progenitors.

Since the mass at high density also increases with increasing central density for the  $\text{C-O}$  progenitor, it appears likely that the difference in central density is important for this increase in the  $\text{C-O-Ne}$  case as well. However, the increase in the mass at high density for the  $\text{C-O-Ne}$  case is more pronounced. This suggests that the central ignition also plays a role. The increase in the IGE yield that results from this higher central density is negligible for the  $\text{C-O}$  case. This is consistent with the results of Krueger et al. (2012), who found that IGE yield is fairly independent of central density. The  $\text{C-O-Ne}$  case, however, appears to act very differently. The mean IGE yield found here

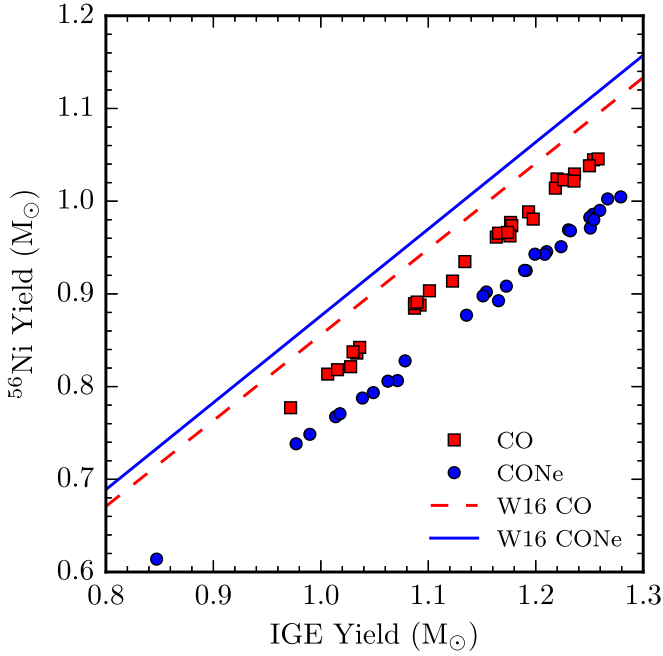


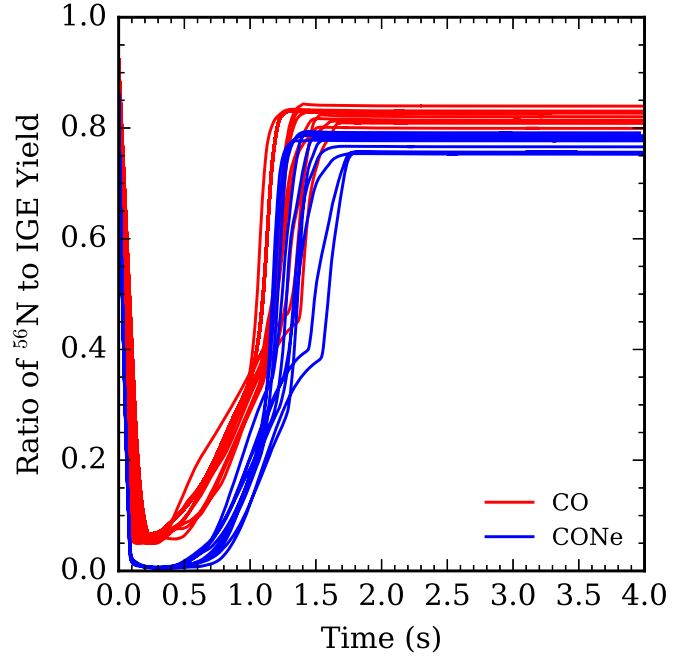
**Figure 5.** Estimated yield of  $^{56}\text{Ni}$  as a function of final mass burned to IGE for  $\text{C-O-Ne}$  progenitors (blue) and  $\text{C-O}$  progenitors (red) at  $t = 4.0$  s. Lines indicate corresponding relations found in Willcox et al. (2016) with a lower central density and  $\text{C-O-Ne}$  progenitor whose interior is not mixed during cooling.

is more than  $0.15 M_{\odot}$  larger than that found in Willcox et al. (2016). This increase closes the gap, making the average IGE yields from the  $\text{C-O}$  and  $\text{C-O-Ne}$  cases similar. The steeper dependence of IGE yield on expansion is partially responsible for this large change, in combination with the larger change in how much expansion happens in the  $\text{C-O-Ne}$  case. This supports both the central density and the location of ignition playing a role in bringing the explosions into a range where  $\text{C-O}$  and  $\text{C-O-Ne}$  cases produce similar amounts of IGE.

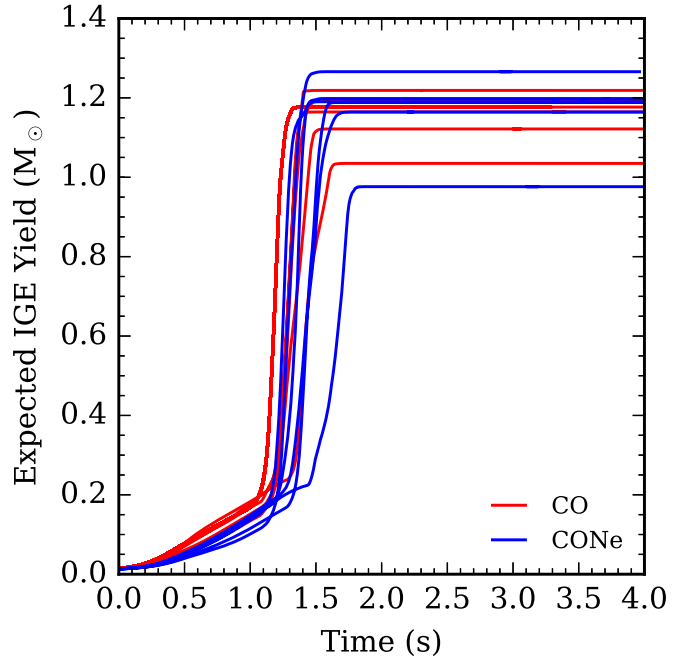
While the higher central density makes the IGE yields quite similar, the hybrid  $\text{C-O-Ne}$  WD still produces less  $^{56}\text{Ni}$  than a  $\text{C-O}$  WD at similar central density. In order to understand this we looked more carefully at how the process of electron capture during the explosion proceeds in our simulations. Again we find that both the central density of the progenitor and the location of ignition are important.

Figure 5 shows the estimated  $^{56}\text{Ni}$  yields across the range of masses burned to IGE for all  $\text{C-O}$  and  $\text{C-O-Ne}$  realizations. The difference between the two sets of results is more pronounced than the difference between  $\text{C-O-Ne}$  and  $\text{C-O}$  models found by Willcox et al. (2016). The results found here, in which the carbon-poor compositions have a lower fractional  $^{56}\text{Ni}$  yield, are more consistent with the expectation for a lower peak burning temperature with lower C abundance. This motivates a closer inspection of how the  $^{56}\text{Ni}/\text{IGE}$  ratio evolves during the explosion.

The evolution of the fraction, by mass, of IGE material expected to be in the form of  $^{56}\text{Ni}$  after freeze-out is shown in Figure 6. The figure presents the results from the same realizations as in Figure 3. The ratios for the yields of explosions from hybrid progenitors are consistently lower than the ratios of yields from traditional progenitors. Figure 7 shows the concurrent evolution of mass burned to IGE for realizations 25–30 from both suites. The total IGE has a mostly similar



**Figure 6.** Expected ratio of  $^{56}\text{Ni}$  to total IGE production by mass vs. time showing the evolution for both suites of simulations. Shown are realizations 21–30. Results from  $\text{C-O-Ne}$  progenitors are in blue and  $\text{C-O}$  progenitors in red.



**Figure 7.** Plot of estimated mass burned to IGEs vs. time showing the evolution for both suites of simulations for realizations 25–30. Results from  $\text{C-O-Ne}$  progenitors are in blue and  $\text{C-O}$  progenitors red.

evolution, and the hybrid results show more scatter, but there is not an obvious difference between the results from the two progenitors. These plots together show that the ratio is the quantity that demonstrates important differences between  $\text{C-O}$  and  $\text{C-O-Ne}$  cases.

During the deflagration phase, the  $\text{C-O}$  models on average burn slightly more material to IGE and also had a significantly higher fraction of IGE material that is  $^{56}\text{Ni}$ , yielding more  $^{56}\text{Ni}$  than the  $\text{C-O-Ne}$  models. This result is counter to that

observed in Willcox et al. (2016). In that work, with a lower density progenitor with a deflagration ignited off-center, the  $\text{C-O}$  mostly showed a smaller fraction of IGE in the form of  $^{56}\text{Ni}$  through most of the deflagration phase. That difference was then closed during the detonation phase, to obtain similar ratios as seen in the lines in Figure 5 above. A similar effect happens here during the detonation phase, but the fraction of material that is  $^{56}\text{Ni}$  stays higher for the  $\text{C-O}$  progenitors.

The differences seen in the deflagration phase in Figure 6 appear to be critical. Central ignition at a higher central density leads to much more electron capture during the deflagration phase for the  $\text{C-O-Ne}$  case. Remarkably, up to around 0.5 s, no  $^{56}\text{Ni}$  is expected to be produced by the  $\text{C-O-Ne}$  progenitor. The comparison to the results of Willcox et al. (2016) indicate that the central ignition, in higher density regions, is important to this outcome. Comparing to the  $\text{C-O}$  progenitor here indicates that the lower energy release may also slow the rise of plumes, allowing more electron capture.

#### 4. Discussion and Conclusion

As mentioned above, we describe the results principally in terms of the yield of the  $^{56}\text{Ni}$ , a proxy for brightness. Our first conclusion is that hybrid progenitors that have experienced mixing during accretion are viable progenitors for type Ia supernovae.  $^{56}\text{Ni}$  yields from simulations in DDT explosion paradigm are consistent with yields inferred from observations, roughly  $0.6 M_{\odot}$ . There is of course considerable scatter in the results and as with other models in the DDT paradigm, these models produce more than  $0.6 M_{\odot}$ , the average being  $0.89 M_{\odot}$ , indicating these would correspond to very bright events.

Going beyond the first-order, our simulations of explosions from these hybrid progenitors gave a lower  $^{56}\text{Ni}$  yield than from similar traditional  $\text{C-O}$  progenitors, a result expected from the earlier study of explosions from unmixed hybrid progenitors (Willcox et al. 2016). We also attribute this difference to the lower C abundance in the hybrid progenitor than in the traditional progenitor.

Comparing the relative abundances of  $^{56}\text{Ni}$  to IGE between the mixed hybrid progenitors and traditional  $\text{C-O}$  models indicated substantial differences, with the hybrid progenitors producing a lower ratio of  $^{56}\text{Ni}$  to IGEs. This difference was particularly pronounced during the deflagration phase of the explosion, and from that we conclude that the evolution of high-density material and the amount of neutronization during the burning at high densities is critical to the evolution and outcome of the explosion.

We were also able to compare the results from these mixed hybrid progenitors to those of the earlier unmixed progenitors. Willcox et al. (2016) reported that compared to the unmixed hybrid progenitors,  $\text{C-O}$  models consistently yielded a greater IGE mass. They interpreted this result as following from the lower  $^{12}\text{C}$  abundance in the hybrid models and the fact that  $^{20}\text{Ne}$ -rich fuel burns to cooler temperatures than the fuel in traditional  $\text{C-O}$  models, which results in slower burning and thus a lower overall IGE yield. Our yields from explosions from the mixed progenitors did not show the same diminution in IGE yield. We attribute this difference to the higher central density required for ignition of these mixed hybrid models. The results of explosions from the mixed hybrid models produced a smaller fraction of IGEs in the form of  $^{56}\text{Ni}$  than the unmixed hybrid case, and we attribute this difference to both the central density and the location, center or off-center, of deflagration

ignition, which determine the amount of electron capture during burning and hence the relative abundance of  $^{56}\text{Ni}$  to IGEs.

To summarize our conclusions, we attribute the following major differences to the progenitor treated here, which is mixed during cooling and centrally ignited, compared to the case in Willcox et al. (2016) that did not mix while cooling:

1. Central ignition enhances the production of IGE.
2. The higher central density necessitated for ignition by the lower central carbon fraction leads to a higher production of IGE as well as stronger electron capture.
3. The off-center ignition used for the  $\text{C-O-Ne}$  progenitor in Willcox et al. (2016) appears to have suppressed electron capture due to the deflagration being more isolated to lower densities.
4. In these mixed hybrid models, electron capture is noticeably enhanced in the  $\text{C-O-Ne}$  case compared to  $\text{C-O}$  at the same density and ignition location.
5. These features together indicate that explosions from  $\text{C-O-Ne}$  progenitors should have similar IGE yields to normal  $\text{C-O}$  progenitors but lower kinetic energies. At the same time,  $\text{C-O-Ne}$  explosions should show lower  $^{56}\text{Ni}$  yield due to enhanced electron capture during the deflagration.

The “punch line” of all this is that hybrid progenitors should produce dimmer explosions, but not as much difference as found in Willcox et al. (2016). We end by noting that the existence of these hybrid WDs is a recent state-of-the-art result from stellar evolution, but our understanding and ability to model stellar evolution is far from complete. These results depend on the details of the convection and those details depend in turn on the presence of the convective Urca process, which is still an outstanding problem subject to ongoing study (Calder et al. 2019; D. P. Willcox et al. 2019, in preparation). The choice of central or off-center ignition is tied to how convective Urca affects the convection before the explosion.

This work was supported in part by the U.S. Department of Energy under grant DE-FG02-87ER40317 and in part by the U.S. National Science Foundation via a supplement to grant AST-1211563. Support also came from the Data + Computing = Discovery summer program at the Institute for Advanced Computational Science at Stony Brook University. The software used in this work was developed in part by the DOE-supported ASC/Alliances Center for Astrophysical Thermonuclear Flashes at the University of Chicago. The authors gratefully thank Josiah Schwab for discussion of the study and comments on the manuscript, this would not have been possible without their kind help. The authors also thank Peter Hoefflich for very helpful discussions of this and related work. The source code used for this study is available as a package compatible with the current FLASH code from <http://astronomy.ua.edu/townsley/code>. Results in this paper were obtained using the high-performance computing system at the Institute for Advanced Computational Science at Stony Brook University.

*Software:* Flash (Calder et al. 2000, 2002; Fryxell et al. 2000; Dubey et al. 2013, 2014) (<http://flash.uchicago.edu/>), MESA (Paxton et al. 2011, 2013, 2015, 2016) (<http://mesa.sourceforge.net/>), The Helmholtz EOS table used in CASTRO (Timmes & Swesty 2000), Available in the public BoxLib



Microphysics repository at (<https://github.com/BoxLib/Codes/Microphysics.git>, commit hash 45ed859b6c1dc80d831d93f9728986d6ad6e1ddc), Matplotlib (<https://doi.org/10.5281/zenodo.44579>).

### ORCID iDs

Carlyn N. Augustine  <https://orcid.org/0000-0002-9741-5987>

Donald E. Willcox  <https://orcid.org/0000-0003-2300-5165>

Dean M. Townsley  <https://orcid.org/0000-0002-9538-5948>

Alan C. Calder  <https://orcid.org/0000-0001-5525-089X>

### References

- Almgren, A. S., Beckner, V. E., Bell, J. B., et al. 2010, *ApJ*, **715**, 1221
- Arnett, W. D., Truran, J. W., & Woosley, S. E. 1971, *ApJ*, **165**, 87
- Bell, J. B., Day, M. S., Rendleman, C. A., Woosley, S. E., & Zingale, M. 2004, *ApJ*, **608**, 883
- Bertola, F. 1964, *AnAp*, **27**, 319
- Bildsten, L., Shen, K. J., Weinberg, N. N., & Nelemans, G. 2007, *ApJL*, **662**, L95
- Blinnikov, S. I., & Khokhlov, A. M. 1986, *SvAL*, **12**, 131
- Bravo, E., Gil-Pons, P., Gutiérrez, J. L., & Doherty, C. L. 2016, *A&A*, **589**, A38
- Brooks, J., Bildsten, L., Marchant, P., & Paxton, B. 2015, *ApJ*, **807**, 74
- Brooks, J., Bildsten, L., Schwab, J., & Paxton, B. 2016, *ApJ*, **821**, 28
- Brooks, J., Schwab, J., Bildsten, L., et al. 2017b, *ApJ*, **850**, 127
- Brooks, J., Schwab, J., Bildsten, L., Quataert, E., & Paxton, B. 2017a, *ApJL*, **834**, L9
- Calder, A. C., Curtis, B. C., Dursi, L. J., et al. 2000, Proceedings of Supercomputing 2000, <http://sc2000.org>
- Calder, A. C., Fryxell, B., Plewa, T., et al. 2002, *ApJS*, **143**, 201
- Calder, A. C., Krueger, B. K., Jackson, A. P., et al. 2017, *Journal of Physics Conference Series*, **837**, 012005
- Calder, A. C., Krueger, B. K., Jackson, A. P., & Townsley, D. M. 2013, *FrPhy*, **8**, 168
- Calder, A. C., & Townsley, D. M. 2019, in *Astrophysical Validation*, ed. C. Beisbart & N. J. Saam (Cham: Springer International Publishing), 685
- Calder, A. C., Townsley, D. M., Seitenzahl, I. R., et al. 2007, *ApJ*, **656**, 313
- Calder, A. C., Willcox, D. E., DeGrendele, C. J., et al. 2019, *Journal of Physics: Conference Series*, **1225**, 012002
- Chamulak, D. A., Brown, E. F., Timmes, F. X., & Dupczak, K. 2008, *ApJ*, **677**, 160
- Chandrasekhar, S. 1981, *Hydrodynamic and Hydromagnetic Stability* (New York: Dover)
- Chen, M. C., Herwig, F., Denissenkov, P. A., & Paxton, B. 2014, *MNRAS*, **440**, 1274
- Denissenkov, P. A., Herwig, F., Truran, J. W., & Paxton, B. 2013, *ApJ*, **772**, 37
- Denissenkov, P. A., Truran, J. W., Herwig, F., et al. 2015, *MNRAS*, **447**, 2696
- Diamond, T. R., Höflich, P., Hsiao, E. Y., et al. 2018, *ApJ*, **861**, 119
- Dubey, A., Antypas, K., Calder, A., et al. 2014, *International Journal of High Performance Computing Applications*, **28**, 225
- Dubey, A., Calder, A., Fisher, R., et al. 2013, *International Journal of High Performance Computing Applications*, **27**, 360
- Fesen, R. A., Höflich, P. A., Hamilton, A. J. S., et al. 2007, *ApJ*, **658**, 396
- Filippenko, A. V. 1997, *ARA&A*, **35**, 309
- Fink, M., Hillebrandt, W., & Röpke, F. K. 2007, *A&A*, **476**, 1133
- Fisher, R., & Jumper, K. 2015, *ApJ*, **805**, 150
- Foley, R. J., Chornock, R., Filippenko, A. V., et al. 2009, *AJ*, **138**, 376
- Fryxell, B., Olson, K., Ricker, P., et al. 2000, *ApJS*, **131**, 273
- Gamezo, V. N., Khokhlov, A. M., & Oran, E. S. 2005, *ApJ*, **623**, 337
- Gamezo, V. N., Khokhlov, A. M., Oran, E. S., Chitcheanova, A. Y., & Rosenberg, R. O. 2003, *Sci*, **299**, 77
- Glasner, S. A., Livne, E., Steinberg, E., Yalinewich, A., & Truran, J. W. 2018, *MNRAS*, **476**, 2238
- Harkness, R. P., & Wheeler, J. C. 1990, in *Supernovae*, ed. A. G. Petschek, **1**
- Hillebrandt, W., Kromer, M., Röpke, F. K., & Ruiter, A. J. 2013, *FrPhy*, **8**, 116
- Hillebrandt, W., & Niemeyer, J. C. 2000, *ARA&A*, **38**, 191
- Höflich, P., Khokhlov, A., Wheeler, J. C., et al. 1996, *ApJL*, **472**, L81
- Höflich, P. 2006, *NuPhA*, **777**, 579
- Höflich, P., Gerardy, C. L., Nomoto, K., et al. 2004, *ApJ*, **617**, 1258
- Höflich, P., & Khokhlov, A. 1996, *ApJ*, **457**, 500
- Höflich, P., Khokhlov, A. M., & Wheeler, J. C. 1995, *ApJ*, **444**, 831
- Howell, D. A. 2011, *NatCo*, **2**, 350
- Hoyle, F., & Fowler, W. A. 1960, *ApJ*, **132**, 565
- Iben, I., Jr., & Tutukov, A. V. 1984, *ApJS*, **54**, 335
- Imshennik, V. S., Filippov, S. S., & Khokhlov, A. M. 1981, *SvAL*, **7**, 121
- Jackson, A. P., Calder, A. C., Townsley, D. M., et al. 2010, *ApJ*, **720**, 99
- Jackson, A. P., Townsley, D. M., & Calder, A. C. 2014, *ApJ*, **784**, 174
- Kashi, A., & Soker, N. 2011, *MNRAS*, **417**, 1466
- Katz, M. P., Zingale, M., Calder, A. C., et al. 2016, *ApJ*, **819**, 94
- Kawai, Y., Saio, H., & Nomoto, K. 1987, *ApJ*, **315**, 229
- Khokhlov, A. M. 1981, *SvAL*, **7**, 410
- Khokhlov, A. M. 1983, *SvAL*, **9**, 160
- Khokhlov, A. M. 1991, *A&A*, **245**, 114
- Khokhlov, A. M. 1995, *ApJ*, **449**, 695
- Kromer, M., Ohlmann, S. T., Pakmor, R., et al. 2015, *MNRAS*, **450**, 3045
- Krueger, B. K., Jackson, A. P., Calder, A. C., et al. 2012, *ApJ*, **757**, 175
- Krueger, B. K., Jackson, A. P., Townsley, D. M., et al. 2010, *ApJL*, **719**, L5
- Kuhlen, M., Woosley, S. E., & Glatzmaier, G. A. 2006, *ApJ*, **640**, 407
- Lattanzio, J. C., Tout, C. A., Neumerzhitskii, E. V., Karakas, A. I., & Lesaffre, P. 2017, *MmSAI*, **88**, 248
- Lecoanet, D., Schwab, J., Quataert, E., et al. 2016, *ApJ*, **832**, 71
- Leibundgut, B. 2001, *ARA&A*, **39**, 67
- Livne, E. 1990, *ApJL*, **354**, L53
- Lorén-Aguilar, P., Isern, J., & García-Berro, E. 2009, *A&A*, **500**, 1193
- Meakin, C. A., Seitenzahl, I., Townsley, D., et al. 2009, *ApJ*, **693**, 1188
- Meng, X., & Podsiadlowski, P. 2014, *ApJL*, **789**, L45
- Meng, X., & Podsiadlowski, P. 2018, *ApJ*, **861**, 127
- Minkowski, R. 1941, *PASP*, **53**, 224
- Niemeyer, J. C. 1999, *ApJL*, **523**, L57
- Niemeyer, J. C., & Woosley, S. E. 1997, *ApJ*, **475**, 740
- Nomoto, K. 1980, *SSRv*, **27**, 563
- Nomoto, K. 1982, *ApJ*, **257**, 780
- Nomoto, K., Thielemann, F.-K., & Yokoi, K. 1984, *ApJ*, **286**, 644
- Nonaka, A., Aspden, A. J., Zingale, M., et al. 2012, *ApJ*, **745**, 73
- Pakmor, R., Edelmann, P., Röpke, F. K., & Hillebrandt, W. 2012a, *MNRAS*, **424**, 2222
- Pakmor, R., Hachinger, S., Röpke, F. K., & Hillebrandt, W. 2011, *A&A*, **528**, A117
- Pakmor, R., Kromer, M., Taubenberger, S., et al. 2012b, *ApJL*, **747**, L10
- Paxton, B., Bildsten, L., Dotter, A., et al. 2011, **192**, 3
- Paxton, B., Cantiello, M., Arras, P., et al. 2013, *ApJS*, **208**, 4
- Paxton, B., Marchant, P., Schwab, J., et al. 2015, *ApJS*, **220**, 15
- Paxton, B., Marchant, P., Schwab, J., et al. 2016, *ApJS*, **223**, 18
- Perlmutter, S., Aldering, G., Goldhaber, G., The Supernova Cosmology Project, et al. 1999, *ApJ*, **517**, 565
- Phillips, M. M. 1993, *ApJL*, **413**, L105
- Pinto, P. A., & Eastman, R. G. 2001, *NewA*, **6**, 307
- Piro, A. L., & Bildsten, L. 2008, *ApJ*, **673**, 1009
- Porter, A. C., & Filippenko, A. V. 1987, *AJ*, **93**, 1372
- Raskin, C., Timmes, F. X., Scannapieco, E., Diehl, S., & Fryer, C. 2009, *MNRAS*, **399**, L156
- Riess, A. G., Filippenko, A. V., Challis, P., et al. 1998, *AJ*, **116**, 1009
- Röpke, F. K., & Sim, S. A. 2018, *SSRv*, **214**, 72
- Saio, H., & Nomoto, K. 1985, *A&A*, **150**, L21
- Saio, H., & Nomoto, K. 2004, *ApJ*, **615**, 444
- Scalzo, R. A., Aldering, G., Antilogus, P., et al. 2010, *ApJ*, **713**, 1073
- Schmidt, W., Niemeyer, J. C., & Hillebrandt, W. 2006a, *A&A*, **450**, 265
- Schmidt, W., Niemeyer, J. C., Hillebrandt, W., & Röpke, F. K. 2006b, *A&A*, **450**, 283
- Schwab, J., & Garaud, P. 2019, *ApJ*, **876**, 10
- Seitenzahl, I. R., & Townsley, D. M. 2017, in *Nucleosynthesis in Thermonuclear Supernovae*, ed. A. W. Alsabti & P. Murdin (Cham: Springer International Publishing), 1955
- Seitenzahl, I. R., Townsley, D. M., Peng, F., & Truran, J. W. 2009, *ADNDT*, **95**, 96
- Shen, K. J., Bildsten, L., Kasen, D., & Quataert, E. 2012, *ApJ*, **748**, 35
- Shen, K. J., Kasen, D., Miles, B. J., & Townsley, D. M. 2018, *ApJ*, **854**, 52
- Siess, L. 2009, *A&A*, **497**, 463
- Sim, S. A., Fink, M., Kromer, M., et al. 2012, *MNRAS*, **420**, 3003
- Sim, S. A., Röpke, F. K., Hillebrandt, W., et al. 2010, *ApJL*, **714**, L52
- Starrfield, S., Iliadis, C., Timmes, F. X., et al. 2012, *BASI*, **40**, 419
- Taam, R. E. 1980a, *ApJ*, **237**, 142
- Taam, R. E. 1980b, *ApJ*, **242**, 749
- Taylor, G. 1950, *RSPSA*, **201**, 192
- Timmes, F. X., & Swesty, F. D. 2000, *ApJS*, **126**, 501
- Timmes, F. X., & Woosley, S. E. 1992, *ApJ*, **396**, 649

- Townsley, D. M., Calder, A. C., Asida, S. M., et al. 2007, [ApJ](#), **668**, 1118
- Townsley, D. M., Jackson, A. P., Calder, A. C., et al. 2009, [ApJ](#), **701**, 1582
- Townsley, D. M., Miles, B. J., Shen, K. J., & Kasen, D. 2019, [ApJL](#), **878**, L38
- Townsley, D. M., Miles, B. J., Timmes, F. X., Calder, A. C., & Brown, E. F. 2016, [ApJS](#), **225**, 3
- Tutukov, A. V., & Iungelson, L. R. 1976, [Afz](#), **12**, 521
- Tutukov, A. V., & Yungelson, L. R. 1979, [AcA](#), **29**, 665
- Vladimirova, N., Weirs, G., & Ryzhik, L. 2006, [CTM](#), **10**, 727
- Wang, B., Meng, X., Liu, D.-D., Liu, Z.-W., & Han, Z. 2014, [ApJL](#), **794**, L28
- Webbink, R. F. 1984, [ApJ](#), **277**, 355
- Weinberg, D. H., Mortonson, M. J., Eisenstein, D. J., et al. 2013, [PhR](#), **530**, 87
- Willcox, D. E., Townsley, D. M., Calder, A. C., Denissenkov, P. A., & Herwig, F. 2016, [ApJ](#), **832**, 13
- Woosley, S. E., & Weaver, T. A. 1994, [ApJ](#), **423**, 371
- Woosley, S. E., Weaver, T. A., & Taam, R. E. 1980, in *Texas Workshop on Type I Supernovae*, ed. J. C. Wheeler, 96
- Woosley, S. E., Wunsch, S., & Kuhlen, M. 2004, [ApJ](#), **607**, 921
- Wunsch, S., & Woosley, S. E. 2004, [ApJ](#), **616**, 1102
- Yoon, S.-C., Podsiadlowski, P., & Rosswog, S. 2007, [MNRAS](#), **380**, 933
- Yuan, F., Quimby, R. M., Wheeler, J. C., et al. 2010, [ApJ](#), **715**, 1338

Q9

